

Unimolecular decomposition of NO₃: The NO+O₂ threshold regime

K. Mikhaylichenko, C. Riehn,^{a)} L. Valachovic, A. Sanov, and C. Wittig

Department of Chemistry, University of Southern California, Los Angeles, California 90089-0482

(Received 13 June 1996; accepted 16 July 1996)

The unimolecular decomposition of expansion-cooled NO₃ has been investigated in the threshold regime of the NO+O₂ channel. Photoexcitation in the region 16 780–17 090 cm⁻¹ (596–585 nm) prepares ensembles of molecular eigenstates, each of which is a mixture of the *B* ²*E'* bright state and lower electronic states. The *X* ²*A*₂' ground state is believed to be the probable terminus of ²*E'* radiationless decay, though participation of *A* ²*E''* is also possible. For these photon energies, unimolecular decomposition occurs exclusively via the NO+O₂ channel, and NO yield spectra and state distributions have been obtained. The yield spectra are independent of the rotational state monitored, as expected for a large reverse barrier. The state distributions are insensitive to the photolysis photon energy and can be rationalized in terms of dynamical bias. The NO yield goes to zero rapidly above the O+NO₂ threshold (17 090±20 cm⁻¹). Because of tunneling, the NO+O₂ channel does not have a precise threshold; the value 16 780 cm⁻¹ is the smallest photon energy that yielded signals under the present conditions. Very small decomposition rates were obtained via time-domain measurements in which reactive quenching of long-lived NO₃ fluorescence was observed. The rates varied from 1×10⁴ at 16 780 cm⁻¹ to 6×10⁷ s⁻¹ at 16 880 cm⁻¹, and their collision free nature was confirmed experimentally. These data were fitted by using a one-dimensional tunneling model for motion along the reaction coordinate combined with the threshold Rice–Ramsperger–Kassel–Marcus (RRKM) rate. The top of the NO+O₂ barrier is estimated to lie at 16 900±15 cm⁻¹. Translational energy measurements of specific NO (*X* ²Π_{Ω,ν,J}) levels showed that O₂ is highly excited, with a population inversion extending to energies above the *a* ¹Δ_g threshold, in agreement with previous work. It is possible that the main O₂ product is *X* ³Σ_g⁻, though some participation of *a* ¹Δ_g cannot be ruled out. Within the experimental uncertainty, *b* ¹Σ_g⁺ is not produced. © 1996 American Institute of Physics. [S0021-9606(96)00240-1]

I. INTRODUCTION

Polyatomic molecules and radicals that exhibit a breakdown of the Born–Oppenheimer approximation and have alternative pathways for unimolecular decay are of great interest in physical chemistry. Detailed studies of such species improve our understanding of how nonadiabatic interactions between zeroth-order electronic potential energy surfaces (PESs) affect the reaction pathways of an excited molecule as it evolves to products. Ultimate goals range from a deeper understanding of the relevant physical and chemical processes to the control of chemical reactivity. In consideration of the above, the nitrate radical (NO₃) provides an excellent model system for examining those aspects of its molecular physics that are involved in chemical change via unimolecular reactions.

Since the discovery of the night-time presence of NO₃ in both the stratosphere¹ and troposphere,² NO₃ has been recognized as an important participant in a growing list of atmospherically relevant chemical transformations (e.g., conversion of NO_x to HNO₃; hydrocarbon and halocarbon oxidation). Furthermore, the photolysis of NO₃ at visible wavelengths is known to yield NO, which contributes to the

catalytic destruction of ozone.³ Appreciation of the atmospheric significance of NO₃ has resulted in numerous spectroscopic and kinetics studies;⁴ however, its absorption spectrum, electronic states, intramolecular dynamics, and photochemistry are not well understood. The main reason that NO₃ has not been more thoroughly investigated experimentally is the difficulty of preparing sufficiently clean, yet intense, beams of cold NO₃ for studies in collision-free environments.

The only low-lying, optically accessible state of NO₃ is *B* ²*E'*. Its absorption features lie at convenient photon energies, and the ²*E'*←²*A*₂' system has a large absorption cross section (σ_{662 nm}=2.2×10⁻¹⁷ cm²).^{5,6} Fluorescence following excitation in the region of 604–678 nm is characterized by diffuse bands^{7,8} and by the Douglas effect.⁹ Namely, the fluorescence lifetimes are much longer than the radiative lifetime of the zeroth-order ²*E'* state (i.e., several hundred microseconds versus ~1 μs, respectively).¹⁰

The three low-lying doublets (i.e., the *X* ²*A*₂' ground state, *A* ²*E''* at 7005 cm⁻¹, and *B* ²*E'* at 15 110 cm⁻¹) are subject to strong nonadiabatic (vibronic) interactions that mix the zeroth-order electronic states.¹¹ Consequently, ²*E'* undergoes internal conversion to a quasicontinuum of near-isoenergetic dark levels, resulting in a dense manifold of molecular eigenstates having mixed ²*E'*/²*A*₂' electronic character, with possible contributions from ²*E''*. As a result, although the wave functions of the optically excited radical

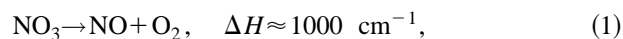
^{a)}Permanent address: Universität Frankfurt a. M., Institut für Physikalische und Theoretische Chemie, Marie-Curie-Str. 11, D-60439 Frankfurt a. M., Germany.

retain some ${}^2E'$ electronic character, they are dominated by the lower electronic manifolds on time scales exceeding the inverse of the mean level spacing, i.e., after any optically prepared coherences have dephased. Note that there is no reason to assume that all members of the full ensemble of molecular eigenstates acquire the same degree of bright character via vibronic interaction, since the most pronounced effect will be to couple levels within the ${}^2E'$ bright-state manifold to dark levels of the same vibronic symmetry. Following the example of NO₂,¹² weaker interactions (second-order spin-orbit and orbit-rotation)¹³ would be responsible for the couplings between levels having different vibronic symmetries.

The nature of the nonadiabatic interactions in NO₃ has been the subject of a number of experimental^{14–17} and theoretical¹⁸ investigations. Briefly, these interactions can be described as: (i) Jahn–Teller (JT) intrastate couplings within the doubly degenerate ${}^2E'$ and ${}^2E''$ electronic states due to doubly degenerate vibrations of e' symmetry (ν_3 and/or ν_4); (ii) linear interstate pseudo-Jahn–Teller (PJT) interactions between ${}^2E'$ and ${}^2A_2'$, due to the ν_3 and/or ν_4 vibrations; (iii) bilinear PJT couplings in ${}^2E'/{}^2E''$ and ${}^2E''/{}^2A_2'$ electronic subsets that symmetrywise require excitation of odd quanta of ν_2 in addition to ν_3 and/or ν_4 . Since a separate treatment of all vibronic coupling mechanisms does not describe a given electronic state correctly, NO₃ presents a complicated multimode vibronic coupling problem.^{11,18,19}

At energies near the ${}^2E'$ origin, were the nuclear motion to transpire exclusively on the ground PES, it would probably be chaotic.²⁰ Since NO₃ has six vibrational degrees of freedom and a vibrational density of states of ~ 100 per cm^{-1} ,²¹ even small coupling matrix elements result in efficient mixing of zeroth-order vibrational levels and are expected to lead to complete intramolecular vibrational redistribution (IVR). Any description of vibronic coupling mechanisms in terms of promoting-mode selection rules can be relevant only at short times, since at longer times the vibrational quantum numbers are destroyed by IVR. Such a hierarchy was suggested as a possible explanation for the structure of the NO₃ laser-induced fluorescence (LIF) spectrum near the ${}^2E' \leftarrow {}^2A_2'$ origin.¹⁴ Specifically, the width of the LIF spectrum indicates that the zeroth-order ${}^2E'$ state survives for only ~ 100 fs, and if this relaxation occurs via levels with promoting-mode character, these levels will decay via IVR into the quasicontinuum of vibrational levels.

Dissociation proceeds via two pathways, with reaction (1) dominating only below the reaction (2) threshold (Fig. 1)



Geometric properties of the reactant and products are shown in Fig. 2.^{17,22,23} Whereas reaction (2) occurs via simple bond fission, reaction (1) involves a three-center mechanism and a tight transition state, i.e., the ground PES correlates to NO+O₂ via a barrier along the reaction coordinate. This barrier presumably arises from an avoided crossing of the ground PES with a repulsive PES correlating to NO+O₂,

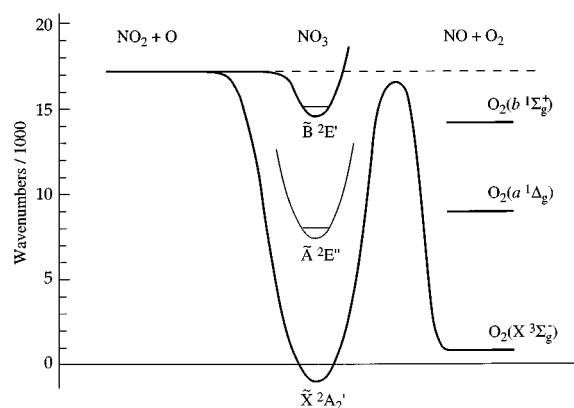


FIG. 1. Energy level diagram showing low-lying NO₃ doublets and energetically accessible O₂ electronic states.

and its presence permits tunneling. In most chemical systems, tunneling of species other than electrons is significant only for hydrogen.²⁴ An example relevant to the present discussion is HFCO, where the HF+CO channel has been observed as much as 2000 cm^{-1} below the barrier.²⁵ Though tunneling probabilities are quite small when larger masses are involved, tunneling will nonetheless dominate as long as competitive decay paths such as spontaneous emission and collisional deactivation are relatively slow. In this regard, due to the very small radiative rates of its individual eigenstates, NO₃ is an ideal candidate to observe heavy-particle tunneling under collision-free conditions.

The narrow NO+O₂ reaction window has been observed recently by using the molecular beams technique to obtain photofragment translational energy distributions.²⁶ Since reaction (1) can contribute to the catalytic destruction of ozone,³ it is important to determine the photon energy range over which it takes place. From the wavelength dependence of the NO time-of-flight (TOF) signal, the reaction (1) barrier was placed at $16\,555 \pm 280 \text{ cm}^{-1}$ and the reaction (2) threshold was found to be $17\,040 \pm 90 \text{ cm}^{-1}$. A NO₃ rotational temperature of ~ 70 K precluded a more precise threshold determination. A substantial yield of O₂ ($X^3\Sigma_g^-$) was ob-

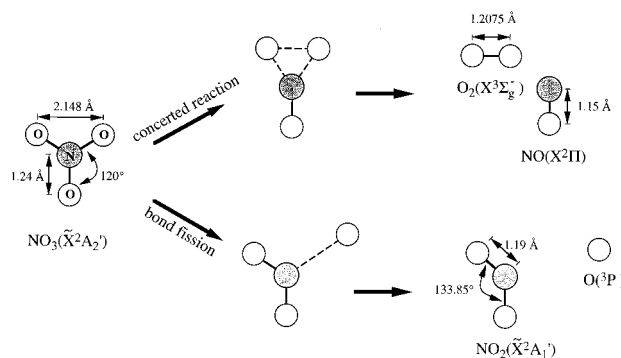


FIG. 2. Schematic diagram showing geometrical properties of NO₃ and reaction products. Molecular parameters are from Ref. 17 (NO₃), Ref. 22 (NO₂), and Ref. 23 (NO and O₂).

served for photolysis below 16 835 cm⁻¹. However, at 17 005 cm⁻¹ the O₂ internal energy distribution was seen to peak at ~13 400 cm⁻¹, suggesting the possible participation of the *a* ¹Δ_g state, which lies 7918 cm⁻¹ above the X ³Σ_g⁻ ground state. Unfortunately, the measurements do not distinguish between high vibrational levels of ³Σ_g⁻ and low vibrational levels of ¹Δ_g.

As the photon energy is increased above the O+NO₂ threshold, *k*₂ quickly exceeds *k*₁. The ²E' surface is believed to correlate to ground state O+NO₂ via a path without an exit barrier, and it has been suggested that reaction (2) might proceed directly via the ²E' surface following photoexcitation.¹⁰ On the other hand, internal conversion to highly excited vibrational levels of the ground PES can be followed by competition between reactions (1) and (2). Even on the ground PES, *k*₂ will eventually dominate with increasing energy due to the qualitatively different transition states. Accordingly, the NO yield spectrum just above the reaction (2) threshold will reflect transition state properties as well as the different couplings.

This paper reports an experimental study of NO₃ unimolecular decay. Photoexcitation in the region 16 530–17 240 cm⁻¹ (605–580 nm) has been used to record LIF spectra of expansion-cooled NO₃ and to initiate its unimolecular decomposition. Reaction mechanisms have been investigated by recording NO yield spectra and state distributions. In addition, collision-free decomposition rates were recorded both by monitoring the NO yield as the pump–probe delay was varied, as well as by monitoring the quenching of the long-lived NO₃ fluorescence. Rates as low as 1×10⁴ s⁻¹ are reported and a tunneling mechanism is implicated. Finally, state-selective center-of-mass (c.m.) translational energy measurements have been used to estimate O₂ internal energy distributions for specific NO (*X* ²Π_Ω, *v*, *J*) levels. The distributions peak ~10 000 cm⁻¹, with at least one-third of the population formed in *X* ³Σ_g⁻ below the *a* ¹Δ_g threshold. This portion displays a population inversion which is most likely vibrational. Though a significant portion of the population lies above the *a* ¹Δ_g threshold, the role of *a* ¹Δ_g versus *X* ³Σ_g⁻ is unclear; it is possible that *X* ³Σ_g⁻ dominates.

II. EXPERIMENTAL ARRANGEMENT

An intense beam of cold NO₃ was developed, based on the pulsed pyrolysis of N₂O₅ using a Chen-type nozzle.²⁷ Ar was bubbled through N₂O₅ cooled to -15 °C (N₂O₅ vapor pressure ~20 Torr; total pressure ~1.1 atm). The resulting 2% N₂O₅/Ar mixture was expanded through a piezoelectrically activated valve (0.5 mm orifice diam) into a resistively heated SiC tube (25 mm×2.2 mm O.D.×1.2 mm I.D.) and then into a low pressure chamber (Fig. 3). Under typical nozzle operating conditions (10 Hz, 500 μs pulse duration) the chamber pressure was <10⁻⁴ Torr, with a base pressure of ~10⁻⁶ Torr. NO₃ production was optimized by adjusting the nozzle temperature while monitoring ²E'←²A'₂' LIF near 662 nm. The present design allowed us to achieve high NO₃ concentrations in the expansion (despite the concomitant production of NO₂) and good rotational cooling.

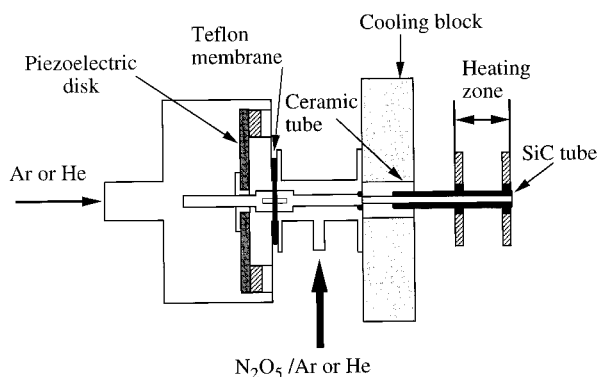


FIG. 3. Schematic diagram of the pulsed pyrolysis nozzle.

Because rotational components of the NO₃ ²E'←²A'₂' spectrum are unassigned, *T*_{tot} was estimated by assuming that cooling is the same as for the coexpanded NO₂. Relative intensities of NO₂ transitions near 16 709 cm⁻¹ [*R*(0)/*R*(2) and *P*(2)/*P*(4)]²⁸ were used, and it was found that Ar carrier cools more efficiently than He carrier (6±1 vs 25±1 K).

The LIF apparatus has been described previously.²⁹ Briefly, a Nd:YAG-pumped dye laser was used to excite NO₃ via the ²E'←²A'₂' system, and the doubled output of an excimer-pumped dye laser was used for LIF detection of NO via the A ²Σ⁺←X ²Π system. The excitation and probe beams were counterpropagated with beam diameters of 2.5 and 1 mm, respectively, in the interaction region. Typical energies were 5–10 mJ for the excitation laser and ~100 μJ for the probe laser.

Since NO₂ has LIF features in the same spectral region as NO₃, a portion of the LIF signal near the opening of the NO+O₂ channel is due to the NO₂ that is present in the expansion. For the NO yield measurements, NO₂ fluorescence was eliminated by using an interference filter. Signal due to NO background in the expansion was an order of magnitude smaller than the NO signal arising from NO₃ photodissociation when probing low NO rotational states (*J* < 3.5). For higher NO rotational levels, signals from the NO background were negligible.

In pump–probe experiments, fluorescence was collected perpendicular to the laser/molecular-beam plane with a photomultiplier tube (PMT) which monitored a 3 mm region along the central portion of the expansion. NO yield spectra were recorded for photon energies in the range of 16 780–17 090 cm⁻¹ and at various delays between the excitation and probe pulses. NO product state distributions were recorded at a pump–probe delay of 350 ns. The probe energy was sufficient to ensure complete saturation for all rotational branches.

Reaction rates were measured by monitoring their quenching of NO₃ fluorescence in real time. The PMT was placed on the expansion axis 30 cm from the interaction region and fluorescence was collected by the photocathode without the use of imaging optics. Scattered laser light was blocked by a filter and NO₃ emission was monitored at

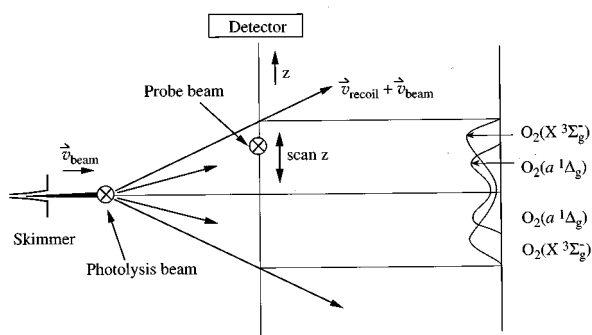


FIG. 4. Schematic diagram of arrangement for correlated NO($^2\Pi_{\Omega}, v, J$) + O₂ distribution measurements. On the right-hand side are examples of the distributions of NO correlated with different O₂ electronic states ($v=0$, $J=0$) assuming a $[X^3\Sigma_g^-]/[a^1\Delta_g]$ ratio of 2.

wavelengths where NO₂ emission is insignificant. This arrangement facilitated monitoring long-lived excited states. The signals reflect both the decay of the excited state and the experimental response function, the latter limiting the estimation of unimolecular decay rates to $\sim 1 \times 10^4 \text{ s}^{-1}$.

The arrangement for measuring correlated NO ($X^2\Pi_{\Omega}, v, J$) + O₂ translational energy distributions is shown in Fig. 4; it is the same as that used to study NO₂ unimolecular decomposition.³⁰ NO₃ is excited in the photolysis region and dissociation takes place as the NO₃ c.m. travels with the molecular beam. After a delay, the products reach the detection region, which is separated spatially from the photolysis region. The NO ($X^2\Pi_{\Omega}, v, J$) fragments that correlate with different O₂ internal energies reach the probe region spatially separated as per their recoil velocities. By scanning the position of the probe beam in the z direction (Fig. 4), spatial profiles of selected NO($X^2\Pi_{\Omega}, v, J$) products were obtained at a pump–probe delay of 2.55 μs . To improve resolution, the photolysis and probe beams were focused to diameters of $\sim 0.2 \text{ mm}$ in their respective interaction regions. NO was detected by 1+1 REMPI, which provides the highest sensitivity possible.³⁰ Data analyses take into account: (i) the fact that each NO recoil profile is a sum of contributions from NO fragments correlated with different O₂ states; and (ii) spatial broadening effects due to the finite sizes of the photolysis and probe beams, the v_z velocity components of parent NO₃ in the molecular beam, the NO₃ rotational temperature, and long dissociation times.^{30,31}

Spatial anisotropy is not expected because of the small NO₃ dissociation rates. The NO signal is observed at all values of $|z|$ smaller than the appearance threshold defined by the recoil velocity and the pump–probe delay. However, due to the geometrical arrangement, spatial profiles for a given $|z|$ have maximum intensity at their furthest displacements from the molecular beam axis, i.e., where the probe beam illuminates the recoil sphere at a grazing angle. This is illustrated by the profiles on the right-hand side of Fig. 4. It is also noted that this arrangement is more sensitive to the slower recoiling products since the two-dimensional number-density of products on the surface of the recoil sphere de-

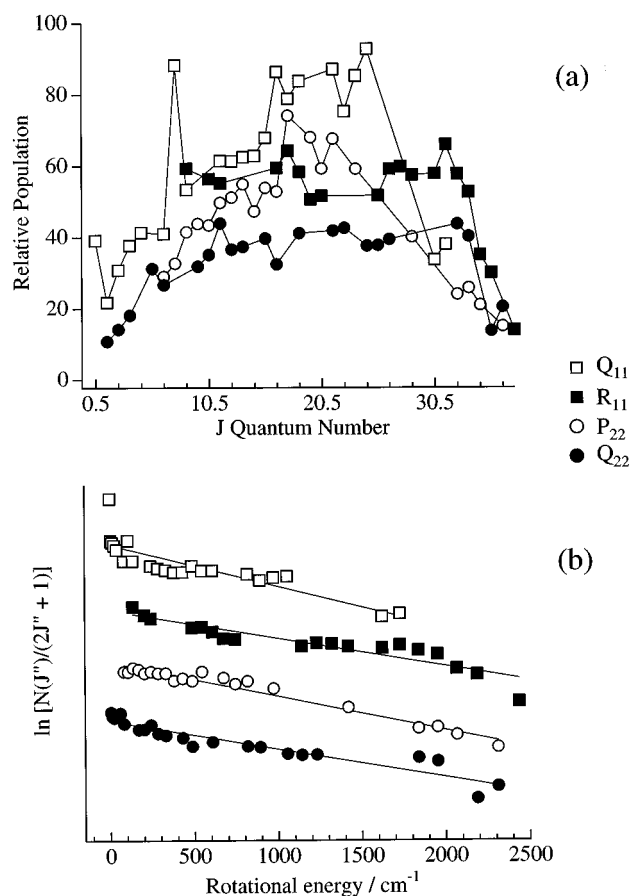


FIG. 5. (a) NO($v=0$) rotational populations for photolysis at $16\,990 \text{ cm}^{-1}$; the lines through the data serve to guide the eye. (b) Boltzmann plots for the data in Fig. 5(a); the lines represent linear fits to the data. All slopes correspond to $1400 \pm 300 \text{ K}$.

creases quadratically with radius, which is proportional to recoil velocity.

III. RESULTS

Photolysis at $16\,990 \text{ cm}^{-1}$ yielded the NO ($X^2\Pi_{1/2,3/2}, v=0$) rotational distributions shown in Fig. 5(a). Vibrational excitation (not shown) is modest, with $\leq 10\%$ of the NO formed in $v=1$. The $^2\Pi_{1/2}$ lower spin–orbit state is slightly more populated than the $^2\Pi_{3/2}$ upper spin–orbit state, and the $A'\Lambda$ -doublet components are slightly more populated than the A'' components. The rotational distributions shown in Fig. 5(a) can be characterized by using the Boltzmann plots shown in Fig. 5(b). The slopes correspond to $1400 \pm 300 \text{ K}$. These slopes should be considered figures of merit rather than temperatures, since they apply to a limited range of rotational levels. NO populations at other photon energies in the range of $16\,840\text{--}17\,000 \text{ cm}^{-1}$ were examined and no significant differences were noted.

Figure 6 shows the NO($X^2\Pi_{1/2}, v=0, J=13.5$) yield spectrum and the NO₃ LIF spectrum recorded just below the NO+O₂ barrier. Since some of the features in the latter are due to NO₂ contamination, a NO₂ LIF spectrum is also shown. Both the NO₃ LIF and the NO yield spectra are in

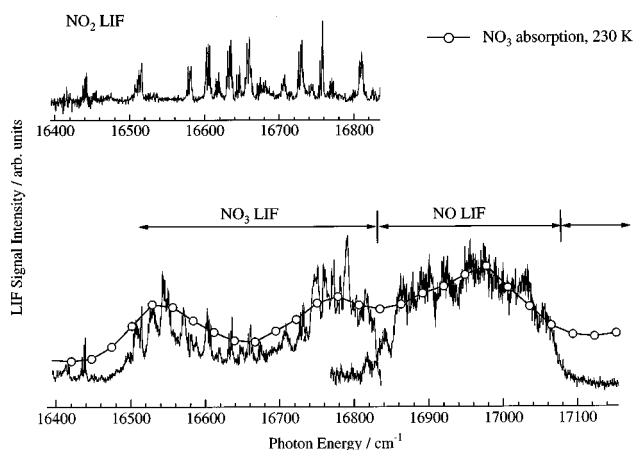


FIG. 6. LIF signals relevant to reaction (1): NO($X^2\Pi_{1/2}$, $v=0$, $J=13.5$) yield spectrum (monitoring R_{11}) at a pump–probe delay of 1 μ s; NO₃ LIF spectrum just below the NO+O₂ barrier (including contaminant NO₂ lines); NO₂ LIF spectrum for $T_{\text{rot}}=6$ K. Also shown (open circles) is the NO₃ 230 K absorption spectrum (Ref. 6).

accord with the 230 K NO₃ absorption profile.⁶ The NO yield spectrum is independent of the rotational state monitored, as expected for a large reverse barrier, and the narrow NO+O₂ reaction window is seen to extend from $16\,820\pm 40$ to $17\,090\pm 20$ cm⁻¹. As in previous studies,²⁴ the largest NO signals were recorded near $16\,980$ cm⁻¹, which corresponds to a peak in the NO₃ absorption.

Below $16\,890$ cm⁻¹, NO buildup is not prompt on the time scale of the nanosecond-resolution pump–probe measurements. In addition, NO₃ fluorescence is also present in this wavelength region. The existence of a *slow* process associated with reaction (1) is illustrated by the time dependence of the NO yield spectra for rotational temperatures of 6 and 25 K, as shown in Fig. 7. For a pump–probe delay of 30 ns, there is an apparent threshold at $16\,878\pm 10$ cm⁻¹. However, upon increasing the pump–probe delay, this threshold is shifted to lower energies. For example, for delays as long as ~ 1 μ s, the threshold drops to $16\,815$ cm⁻¹. For delays longer than ~ 1 μ s, the excited molecules are transported out of the probe region as per the molecular beam velocity. Also, because of the large translational energy release in the exit channel, NO recoil out of the probe region is significant. Thus, monitoring NO buildup times provides an upper limit to the decomposition rates.

The slow unimolecular decay rates described above were also observed via their reactive quenching of the long-lived NO₃ emission. Time resolved emission profiles were obtained at several photon energies, as shown in Fig. 8. Fluorescence quenching was evident above $16\,780$ cm⁻¹ and unimolecular decay rates larger than 1×10^4 s⁻¹ could easily be discerned [Fig. 8(c)]. As the photon energy was increased, reactive quenching of the fluorescence increased rapidly [Figs. 8(a) and 8(b)]. At still larger photon energies, measurement of excited state lifetimes was limited by the 30 ns experimental resolution. Since the decay curves contain contributions from both the NO₃ fluorescence and the apparatus

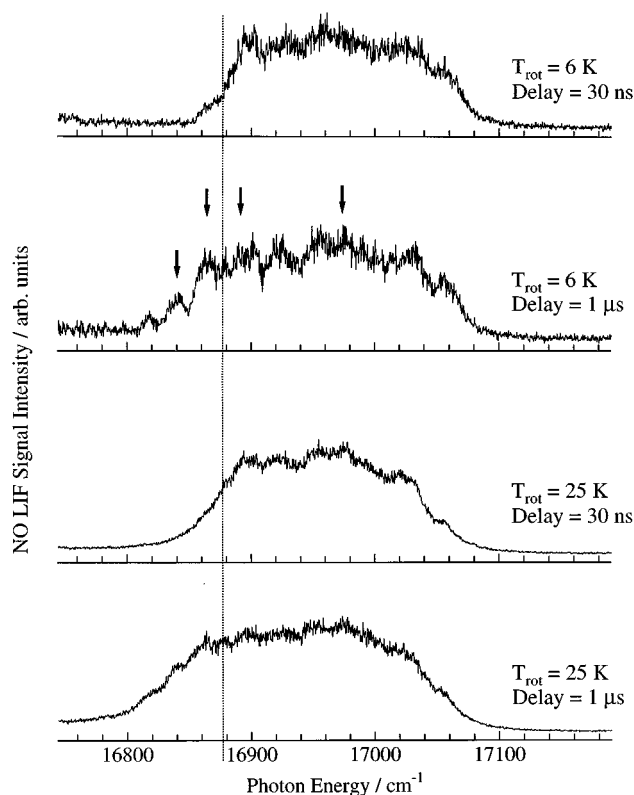


FIG. 7. NO($X^2\Pi_{1/2}$, $v=0$, $J=13.5$) yield spectra at the indicated pump–probe delay times for NO₃ rotational temperatures of 6 and 25 K. Apparent thresholds for $T_{\text{rot}}=6$ and 25 K and 30 ns delay are shown as a vertical dotted line. Arrows indicate the photon energies at which correlated NO ($^2\Pi_{\Omega}$, v, J)+O₂ distributions were obtained.

response function, the deconvolution of the unimolecular decay rates from the measured traces was done assuming biexponential behavior. Moreover, the fit was sensitive to parameters such as the baseline and zero of time used in the fitting procedure. As a result, the estimated uncertainty for each of the k_1 values is $\pm 50\%$.

Figure 9 displays k_1 versus photon energy. The rates extracted from the fast components of the decay curves are indicated by open circles and squares. The open circles represent $T_{\text{rot}}=6$ K. These rates increase from 1×10^4 s⁻¹ at $16\,780$ cm⁻¹ to 6×10^7 s⁻¹ at $16\,880$ cm⁻¹. The squares represent $T_{\text{rot}}=20$ K (350 Torr nozzle backing pressure, 5 Hz operation). Under these conditions the chamber pressure is $<10^{-5}$ Torr, which is an order of magnitude lower than under the $T_{\text{rot}}=6$ K conditions, thus minimizing beam–gas collisions. The higher value of T_{rot} appears to shift the data to slightly lower photon energies without changing the overall trend. In fact, the shift is comparable to the change in the average parent rotational energies in going from 6 to 20 K. The fact that lowering the backing pressure does not affect the slow reaction is consistent with the collision-free nature of this process.

Spatial distributions of specific NO quantum states were obtained for the photon energies indicated by arrows in Fig. 7. A representative profile obtained at $16\,992$ cm⁻¹ is shown

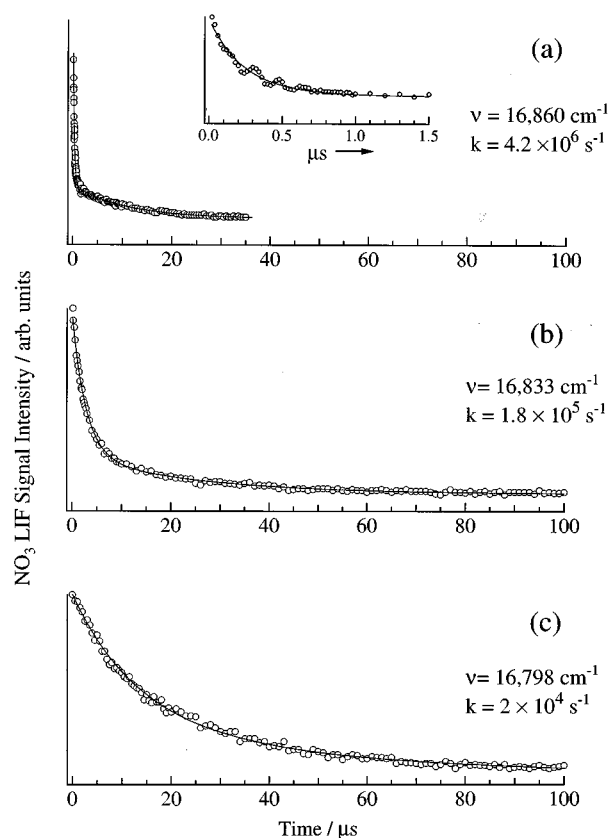


FIG. 8. Time resolved NO₃ emission at the given excitation energies. The lines represent biexponential fits to the data. Also shown are the NO₃ unimolecular decay rates extracted from the fast component of the fluorescence decay curves.

in Fig. 10. The bottom axis indicates the displacement of the monitored NO along the z axis at a pump-probe delay of 2.55 μs . The top axes indicate the appearance thresholds for O₂ electronic and vibrational levels without accounting for

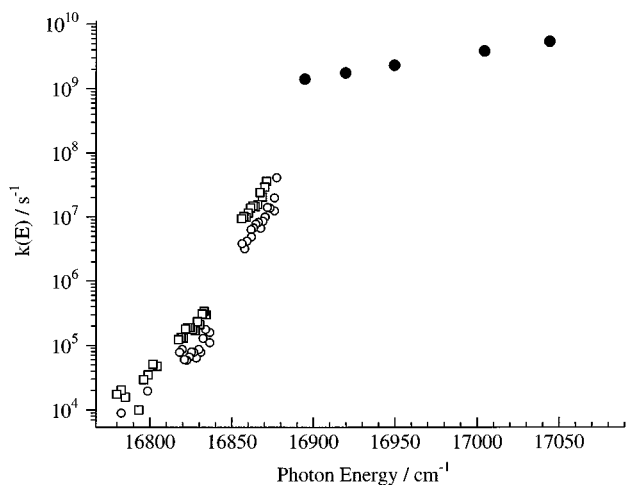


FIG. 9. NO₃ decomposition rate vs photon energy. Open circles and squares represent data obtained by monitoring time resolved NO₃ emission for $T_{\text{rot}}=6$ and ~ 20 K, respectively. Filled circles represent data obtained by using the picosecond-resolution pump-probe technique averaged over the 60 cm^{-1} linewidth of the ultrafast laser (Ref. 44).

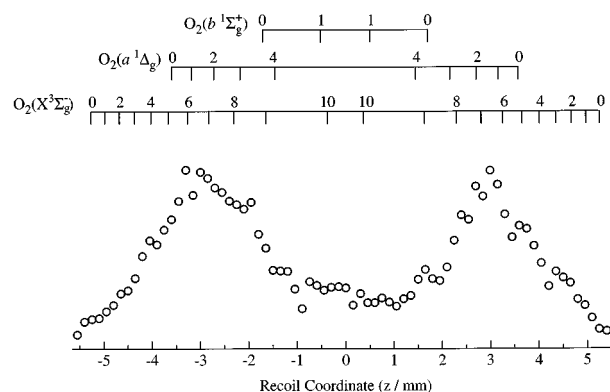


FIG. 10. NO($X^2\Pi_{3/2}$, $v=0$, $J=17.5$) spatial profiles obtained at 16 992 cm^{-1} by monitoring the $A^2\Sigma \leftarrow X^2\Pi_{2/2}$ transition. The bottom axis gives the distance between the centers of the probe and photolysis beams along the z axis; the top axis lists O₂ internal energies.

experimental broadening. Note that the signal associated with O₂($X^3\Sigma_g^-, v=0$) is small. For shorter recoil distances, the signal increases gradually, peaking in the vicinity of the appearance threshold for O₂ internal energies of $\sim 10\,000$ cm^{-1} . Although this internal energy is sufficient to access the $a^1\Delta_g$ state, no abrupt signal increase is observed near the $a^1\Delta_g$ threshold. In addition, the integrated intensity of the signal arising from NO with enough translational energy to preclude $a^1\Delta_g$ formation accounts for a significant fraction of the total (at least one-third). Thus, the data indicate that O₂($X^3\Sigma_g^-$) is formed with a population inversion. Similar results were obtained at 16 863 and 16 892 cm^{-1} , and when monitoring different NO rotational and spin-orbit states.

At 16 841 cm^{-1} , the NO($X^2\Pi_{3/2}$, $v=0$, $J=17.5$) spatial profile corresponds to a larger relative population of the lower O₂($X^3\Sigma_g^-$) levels. However, k_1 is so small ($\sim 2 \times 10^5$ s^{-1}) that NO buildup is comparable to the maximum pump-probe delay of 3 μs allowed by the dimensions of the apparatus and the product recoil, thus complicating analyses. This preliminary result will be the subject of future work.

IV. DISCUSSION

A. The roles of the $X^2A'_2$, A^2E'' , and B^2E' states

Nelson *et al.* used the integrated absorption coefficient of the $^2E' \leftarrow ^2A'_2$ origin to estimate the spontaneous emission lifetime of the zeroth-order $^2E'$ state, obtaining a value of ~ 1 μs .¹⁰ We confirmed this by using a well-established procedure.^{32,33} They also reported long fluorescence lifetimes ($\tau_{\text{fl}} \sim 340$ μs) at the $^2E'$ origin (with some evidence for non-exponential decay at shorter times), indicating an oscillator strength dilution factor of ~ 340 for the observed levels, which span a region of ~ 50 cm^{-1} around the origin. Thus, in this energy range, ~ 7 vibronic levels per cm^{-1} (i.e., $340 \div 50$) are mixed with the $^2E'$ bright state, which is considerably less than the estimated density of $^2A'_2$ vibrational levels ($\sim 100/\text{cm}^{-1}$).³⁴

On the basis of a dilution factor of ~ 340 , it follows that the $^2E' \leftarrow ^2A'_2$ oscillator strength is not distributed statisti-

cally among all nearby levels, in which case the dilution factor would be much larger. Such modest dilution can be rationalized if the matrix elements connecting levels of different vibronic symmetries are smaller than typical energy separations between the levels. However, by analogy with NO₂, where second-order spin-orbit and orbit-rotation matrix elements have been found to be several tenths of a wave number,¹³ at least *some* coupling between levels of different vibronic symmetries is expected, though oscillator strength may be distributed inhomogeneously among the different vibronic species.

Since it has not been possible to fully quantify the extent of dilution or to establish radiationless decay mechanisms, the relative ²E'' and ²A₂' contributions remain unknown. However, ²E'/²A₂' coupling has been confirmed both experimentally¹⁴⁻¹⁷ and theoretically,¹⁸ and ²E'/²E'' coupling is believed to be a higher-order process.^{18,19} Also, ²A₂' is preferred over ²E'' on statistical grounds, i.e., at the present energies, the vibrational level density within the ²A₂' manifold is significantly larger than that within the ²E'' manifold. Thus, we *assume* that ²A₂' is the main terminus of radiationless decay, though participation of ²E'' cannot be ruled out. The conclusions presented below would not be altered seriously by including ²E''.

B. Intramolecular dynamics

At the energies and vibrational state densities of interest in the present study, it is highly probable that the nuclear dynamics would be chaotic even if they were to transpire solely on the ²A₂' zeroth-order PES, i.e., ignoring vibronic interactions. This assumption is based on the exhaustive body of experimental and theoretical data that has accrued in the area of intramolecular vibrational dynamics.²⁰ However, vibronic interactions are known to efficiently promote chaotic dynamics within the vibronic manifolds.^{11,35,36} Therefore we assume that the system displays full vibronic chaos for the energies and time scales of interest in the present study, as was found to be the case for NO₂.^{12,37} Since couplings between different vibronic species are weaker than the couplings within each vibronic manifold, the system can be vibronically chaotic (i.e., within each manifold) without being rovibronically chaotic (i.e., between manifolds). However, again by invoking analogy with NO₂, where it has been reported that rovibronic chaos exists just below *D*₀ as a consequence of second-order spin-orbit and orbit-rotation interactions,¹³ there exists the possibility that NO₃ is rovibronically chaotic.

C. Optical excitation

The vibronic interactions that mix the zeroth-order electronic states provide a means of optically preparing vibrationally excited states that decay via one or more unimolecular decomposition mechanisms. For example, reaction (1) results from weak couplings between the optically prepared molecular eigenstates³⁸ and the NO+O₂ continuum. From the 50 cm⁻¹ width of the ²E'←²A₂' origin LIF feature and the dilution of the oscillator strength, it follows that the mo-

lecular eigenstates have little ²E' character. Instead, they are dominated by the lower electronic manifolds, tentatively assumed to be ²A₂'

$$|\psi_i\rangle = \sum_n \langle {}^2E', v_n | \psi_i \rangle | {}^2E', v_n \rangle + \sum_m \langle {}^2A_2', v_m | \psi_i \rangle | {}^2A_2', v_m \rangle, \quad (3)$$

where $|\psi_i\rangle$ is a molecular eigenstate, the sums over v_n and v_m include all vibrational levels (rotational quantum numbers are suppressed), and $m \gg n$ because of the different vibrational level densities for the ²E' and ²A₂' manifolds. Note that the term "molecular eigenstate" is used even when these levels are coupled weakly to a continuum.

For the tunneling regime examined in the present experiments, all of the measured k_1 values are $< 10^8$ s⁻¹, which corresponds to Lorentzian widths < 0.0005 cm⁻¹. Because of the narrowness of these widths, the energy level structure can be treated as a quasicontinuum of isolated (nonoverlapping) resonances. The high degree of spectral overlap observed experimentally is due to several factors: congestion caused by the many different rotational levels excited when using 6 K samples, the Doppler effect in unskimmed expansions, and the laser linewidth. However, these factors do not lead to quantum interferences, so the approximation of isolated resonances is still valid insofar as the statistical properties of the decay widths is concerned.

Though the decay widths of individual resonances fluctuate about a mean value,³⁹ the present conditions ensure that a large number of resonances are excited by the laser pulse. Thus, fluctuations between measured k_1 values were neither anticipated nor observed. Moreover, coherences imparted by the photoexcitation step dissipate quickly on the time scale of the rate measurements. Thus, we believe that the excited ensemble of levels can be modeled as decaying incoherently with a distribution of rates. It is the relaxation of this optically prepared ensemble that we record as k_1 . The unimolecular decomposition was taken to be single exponential because, within the present experimental uncertainty, it fits. However, there is no theoretical basis for this, and higher quality data may reveal deviations from single-exponential decay.

Photoexcitation does not access the full manifold of molecular eigenstates equivalently. In the absence of saturation, it excites levels in proportion to the squares of their electric dipole matrix elements, and is thus biased. Nonetheless, it is expected that *measured* $k_1(E)$ values differ little from $k_1(E)$ values averaged over *all* molecular eigenstates within the same energy window. The reason is that the reaction rates are not characteristic of the ²E' surface, which carries the oscillator strength but is unreactive toward NO+O₂.¹⁰ Since the ²E' surface contributes little to the makeup of individual eigenstates, as seen by its small weighting coefficient in the expansion of the wave function, the distribution of decay rates is expected to be almost independent of the bright-state contribution to the molecular eigenstate.

D. Reaction rates

It follows from the above arguments that reaction (1) can be described as proceeding via the ground PES and that statistical rate models can be applied which: (i) are semiclassical in nature [e.g., RRKM, phase space theory (PST), statistical adiabatic channel model (SACM)] when the resonances are averaged over;^{40–42} and (ii) exhibit distributions of decay rates, level spacings, absorption strengths, etc., when the resonances are resolved.^{39,43} This picture can be comprised when reactions (1) and (2) compete, specifically, when the latter occurs so rapidly that decay to and within the lower electronic manifolds is incomplete on the time scale of that reaction.

As indicated in Fig. 9, there is no precise reaction (1) threshold—nor, because of the inevitable participation of tunneling, can there be one. The marked variation of k_1 with photon energy shown in Fig. 9 has been verified by repeated measurements and by using two complementary experimental techniques. Namely, rates obtained by monitoring reactive quenching of the NO₃ fluorescence are consistent with rates obtained by recording NO buildup times, though the latter are limited to values $\geq 10^6$ s⁻¹. Also, the *collision-free* nature of this slow unimolecular process was confirmed experimentally.

NO₃ decay rates above the reaction (1) barrier have been reported by Davis *et al.*,⁴⁴ who used the picosecond-resolution pump–probe technique to record NO buildup times. They found that in the ~ 200 cm⁻¹ window between the top of the barrier and the O+NO₂ threshold, k_1 varied from 1 to 5×10^9 s⁻¹, with each measurement averaging rates over the broad (60 cm⁻¹) linewidth of the photolysis laser. These data were fitted by using RRKM theory with a lowest transition state frequency of 70 cm⁻¹.

Figure 9 shows that below the barrier, k_1 varies *much* more rapidly than it does above the barrier, changing by three orders of magnitude in ~ 100 cm⁻¹. Since small tunneling probabilities display near-exponential dependencies on the area beneath the top of the barrier, such rapid variation is expected. Moreover, tunneling can account for the very different slopes that characterize the regimes above and below $\sim 10^9$ s⁻¹ (Fig. 9).²⁶

The simplest way to incorporate tunneling into the statistical model is via motion along a one-dimensional reaction coordinate that is separable at the transition state from the orthogonal degrees of freedom. The tunneling probability can then be calculated by using the WKB approximation,^{45,46} with the potential along the reaction coordinate taken as an inverted parabola. The resulting expression is⁴⁶

$$P(E') = \frac{\exp(-2\pi E'/\omega_b)}{1 + \exp(-2\pi E'/\omega_b)}, \quad (4)$$

where ω_b is the magnitude of the imaginary frequency of the barrier and E' is the energy in the reaction coordinate *below* the zero point of the transition state (i.e., $E' > 0$). To obtain ω_b , it is necessary to have the barrier width and the effective

mass, parameters which are not known. However, we note that a value of $\omega_b = 300$ cm⁻¹ (corresponding to a ~ 1 Å width 100 cm⁻¹ below the top of the barrier and an 8 amu effective mass) yields rates that are consistent with the data shown in Fig. 9.

As mentioned above, the NO yield spectrum near the reaction (2) threshold reflects the k_1/k_2 ratio. Whereas reaction (1) proceeds via the ${}^2A'_2$ ground state, the ${}^2A'_2$ and ${}^2E'$ surfaces can both contribute to reaction (2). It is also possible that ${}^2E''$ participates. It is a daunting task to establish the respective roles of the different PESs involved in reaction (2).

An important point can be made concerning the possible role of ${}^2E'$; namely, were a unimolecular reaction to proceed exclusively on the zeroth-order ${}^2E'$ surface, its threshold rate would be $(h\rho)^{-1} \sim 10^{12}$ s⁻¹, as estimated by using the ρ value of 0.03/cm⁻¹ obtained by direct count.⁴⁷ This is too slow to overcome internal conversion, which occurs with a rate of $\sim 10^{13}$ s⁻¹, as estimated from the width of the ${}^2E'$ original LIF feature. Moreover, for reaction rates $> 10^{12}$ s⁻¹, the transition state will tighten with increasing energy, preventing the rate from rising as rapidly with energy as predicted by a very loose transition state. Thus, it seems unlikely that unimolecular reaction exclusively via the ${}^2E'$ surface can dominate in the k_2 threshold region.

Another extreme case is when reactions (1) and (2) both proceed via the ground state surface. This would occur in the event that internal conversion went to completion prior to reaction. In the rate equation limit, the NO yield above the reaction (2) threshold is then determined by the k_1/k_2 ratio, with each of the rates given by

$$k = \frac{N^\ddagger(E - E_0)}{h\rho(E)}, \quad (5)$$

where $N^\ddagger(E - E_0)$ is the number of open channels at the transition state and $\rho(E)$ is the parent density of states. For a common intermediate, $\rho(E)$ is the same for both decomposition paths, and therefore k_1/k_2 is the ratio of the numbers of open channels at the transition states for reactions (1) and (2), respectively. Since the reaction (1) transition state is tight, its levels can be described as vibrational. Though the frequencies are uncertain, values of 70 and 140 cm⁻¹ for the two lowest transition state frequencies yielded $k_1(E)$ values in agreement with the experimental results.⁴⁴ This predicts an increase in k_1 by a factor of several within a 100 cm⁻¹ energy interval near the O+NO₂ threshold. On the other hand, since the reaction (2) transition state is loose, k_2 will increase rapidly with energy relative to k_1 , leading to the rapid dominance of reaction (2).

At this point, we have not been able to draw firm conclusions concerning the roles of the zeroth-order PESs insofar as reaction (2) is concerned. An obvious extension of the present work is double-resonance experiments in which the reaction (2) threshold regime is examined with good energy resolution and dissociation via the ground PES is decoupled from the radiationless decay step.

E. NO product state distributions and yield spectra

The NO product state distributions can be rationalized by invoking dynamical bias, namely, since the NO+O₂ reverse barrier is large, product excitations are strongly influenced by the transition state region and the exit channel. As anticipated for a large reverse barrier, the NO excitations are insensitive to the photolysis photon energy in the small energy range between the top of barrier and the reaction (2) threshold. The absence of a significant NO ($v \geq 1$) population can be understood as vibrational adiabaticity from the transition state to products. Specifically, vibrational quantum numbers in degrees of freedom orthogonal to the reaction coordinate are conserved past the transition state and appear in the fragments. The predominance of NO ($v=0$) suggests that the N–O bond lengths do not differ significantly between the transition state region and free NO. It is also consistent with the stiffness of the N–O stretch coordinate in the exit channel.

The present work provides characterization of the threshold regions of reactions (1) and (2). Much of this information is obtained from NO yield spectra (Fig. 8), whose spectral density is nearly continuous, albeit with a lumpiness that resembles the NO₃ LIF spectra but with poorer resolution.¹⁴ The NO yield spectrum on the low energy side reflects the threshold region of reaction (1), which proceeds *through* the barrier at the lowest energies. On the high energy side, the yield spectrum reflects competition between reactions (1) and (2).

F. Internal excitations

The data shown in Fig. 10 provide qualitative information concerning O₂ internal excitations despite the low resolution. First, the amount of signal associated with O₂ internal energies lying below the $a^1\Delta_g$ threshold is significant. This can only derive from $X^2\Sigma_g^-$ rovibrational excitation. Recall that correcting the raw data shown in Fig. 10 for the R^2 factor (where R is the radius of the recoil sphere) only *enhances* the large- z contribution.^{30,31} Thus, $X^3\Sigma_g^-$ is definitely produced as a counterfragment of the monitored NO level. The monotonic increase of the signal up to the $a^1\Delta_g$ threshold indicates a considerable population inversion within the $X^3\Sigma_g^-$ ground electronic state.

In the region where $X^3\Sigma_g^-$ and $a^1\Delta_g$ are both energetically accessible, their separate contributions cannot be resolved. However, the decrease in signal in the spatial region close to the center of the recoil sphere (i.e., where $b^1\Sigma_g^+$ would appear) is clear. Combined with the fact that the experimental method is most sensitive to slow fragments, this observation rules out significant population of the $b^1\Sigma_g^+$ state.

Smith *et al.*⁴⁸ have shown that the O+NO₂→O₂+NO bimolecular reaction (300 K) yields O₂ ($X^3\Sigma_g^-$) in high vibrational levels. They report a monotonic decrease in population from $v=6$ to $v=11$, i.e., for O₂ internal energies above 9800 cm⁻¹. Lower vibrational levels could not be detected by using the LIF method they employed, and it was not possible to isolate the respective roles of direct reaction

versus reaction via the NO₃[‡] intermediate. Since O+NO₂ collisions can form NO₃[‡] efficiently, there is the possibility that the observed $X^3\Sigma_g^-$ vibrational levels derive, at least in part, from NO₃ unimolecular decomposition.

The data shown in Fig. 10 indicate a monotonically decreasing population for O₂ internal energies above ~10 500 cm⁻¹. This corresponds to $X^3\Sigma_g^-$ vibrations from $v=6$ or 7 to $v=11$, though, as stated above, neither our measurements nor those of Davis *et al.*²⁴ resolve the separate contributions from $X^3\Sigma_g^-$ and $a^1\Delta_g$. The data of Davis *et al.* are of superior resolution, showing some vibrational structure, whereas the present results are product state selective. However, the two data sets are consistent and the correspondence between the translational energy distributions and the $X^3\Sigma_g^-$ LIF measurements is striking. We interpret this as supporting a major, if not dominant, role for the $X^3\Sigma_g^-$ state.

If the O₂ internal excitation resides predominantly in $X^3\Sigma_g^-$, there is probably a significant *vibrational* population inversion, since it is unlikely that rotations would be excited to such a large extent. This can be rationalized by a reaction (1) transition state having a long O–O bond relative to free O₂. However, though we would have no difficulty *accepting* a $X^3\Sigma_g^-$ vibrational distribution peaked near $v=6$ or 7 based on this mechanism, there currently exists no basis for independent support, for example, through theoretical calculations.

V. CONCLUSIONS

This paper reports and discusses measurements of NO₃ unimolecular reactions under collision-free conditions. A number of complementary data are presented: NO product yield spectra; NO₃ LIF spectra; NO rotational and fine-structure state distributions; rates of NO₃ decomposition; and O₂ internal energies correlated with a specific NO ($X^2\Pi_{\Omega}, v, J$) state. The NO₃ intramolecular dynamics are strongly influenced by nonadiabatic interactions in the $B^2E'/A^2E''/X^2A'_2$ electronic subset.¹⁴ Nuclear motions at these energies are believed to be chaotic, resulting in decomposition rates that can be calculated by using statistical theories.

The NO+O₂ channel involves molecular eigenstates having modest $^2E'$ character, and dominant character of lower electronic manifolds. The most probable terminus of radiationless decay is believed to be $^2A'_2$, but we leave open the possibility of $^2E''$ participation.

A narrow window exists for the NO+O₂ channel. Very slow rates were observed after excitation with photons that promote the system to energies that lie *below* the reaction (1) barrier. Specifically, rates for collision-free photoinitiated unimolecular decomposition ranged from 1×10^4 s⁻¹ at 16 780 cm⁻¹ to 6×10^7 s⁻¹ at 16 880 cm⁻¹. Tunneling is believed to be responsible for this behavior. A simple extension of RRKM theory confirms that tunneling could indeed result in unimolecular decay rates that vary rapidly enough with energy to be consistent with the experimentally measured rates.

NO rotational excitation is modest and the distributions are insensitive to the excitation photon energy. Vibrational excitation is also modest: $[v = 1]/[v = 0] \sim 0.1$. There is a high degree of O₂ internal excitation, with the $X^3\Sigma_g^-$ ground state produced throughout the entire photolysis region, in agreement with results from previous measurements of c.m. translational energy distributions.²⁴ A significant fraction (at least one-third) of the O₂ is formed with internal energies below the $a^1\Delta_g$ threshold, and it is assumed that excitation within $X^3\Sigma_g^-$ is predominantly vibrational as opposed to rotational. The distribution within $X^3\Sigma_g^-$ indicates a population inversion which can be rationalized as due to the geometry of the 3-center transition state.

If O₂($a^1\Delta_g$) is *not* produced, the most populous $X^3\Sigma_g^-$ vibrational levels are $\sim v=6$ or 7 for the photolysis region 16 860–17 080 cm⁻¹. It is important to keep in mind that the measurements do not distinguish between low-lying vibrational levels within $a^1\Delta_g$ and high vibrational levels of $X^3\Sigma_g^-$. Nonetheless, there is a good possibility that $X^3\Sigma_g^-$ is the dominant O₂ species. For example, Smith *et al.*⁴⁸ report that O₂ from the O+NO₂→NO+O₂ reaction is formed in vibrational levels whose populations decrease monotonically from $v=6$ to $v=11$. The O₂ internal energy distribution (see Fig. 10) also decreases monotonically over this range, further supporting O₂($X^3\Sigma_g^-$) as a major (if not dominant) O₂ species.

Above the O+NO₂ threshold, reaction (2) dominates. Though $^2E'$ is believed to correlate without a barrier to ground state products, unimolecular reaction exclusively on $^2E'$ is not fast enough to bypass internal conversion. Specifically, the estimated k_2 value is an order of magnitude smaller than the radiationless decay rate of 10¹³ s⁻¹ inferred from the LIF spectrum of the $^2E' \leftarrow ^2A'_2$ origin. Therefore, several surfaces may contribute. It is a daunting task to establish the respective roles of the different PESs involved in reaction (2).

ACKNOWLEDGMENTS

We thank D. Arnold, P. Ionov, I. Bezel, H. Reisler, I. W. M. Smith, and F. Davis for valuable input.

- ¹J. F. Noxon, R. B. Norton, and W. R. Henderson, *Geophys. Res. Lett.* **5**, 675 (1978).
- ²U. Platt, D. Perner, A. M. Winer, G. W. Harris, and J. N. Pitts, Jr., *Geophys. Res. Lett.* **7**, 89 (1980).
- ³R. A. Graham and H. S. Johnston, *J. Phys. Chem.* **82**, 254 (1978).
- ⁴R. P. Wayne *et al.*, in *The Nitrate Radical: Physics, Chemistry, and the Atmosphere*, Atmospheric Environment Vol. 25A, edited by R. P. Wayne (Pergamon, Oxford, 1991), pp. 1–206.
- ⁵S. P. Sander, *J. Phys. Chem.* **90**, 4135 (1986).
- ⁶R. J. Yokelson, J. B. Burkholder, R. W. Fox, R. K. Talukdar, and A. R. Ravishankara, *J. Phys. Chem.* **98**, 13144 (1994).
- ⁷H. H. Nelson, L. Pasternack, and J. R. McDonald, *J. Phys. Chem.* **87**, 1286 (1983).
- ⁸B. Kim, P. L. Hunter, and H. S. Johnston, *J. Chem. Phys.* **96**, 4057 (1992).
- ⁹A. E. Douglas, *J. Chem. Phys.* **45**, 1007 (1996).
- ¹⁰H. H. Nelson, L. Pasternack, and J. R. McDonald, *J. Chem. Phys.* **79**, 4279 (1983).
- ¹¹H. Köppel, W. Domcke, and L. S. Cederbaum, *Adv. Chem. Phys.* **57**, 59 (1984).
- ¹²A. Delon, R. Georges, and R. Jost, *J. Chem. Phys.* **103**, 7740 (1995).

- ¹³A. Delon, P. Dupré, and R. Jost, *J. Chem. Phys.* **99**, 9482 (1993).
- ¹⁴L. Valachovic, C. Riehn, K. Mikhaylichenko, and C. Wittig, *Chem. Phys. Lett.* (in press).
- ¹⁵A. Weaver, D. W. Arnold, S. E. Bradforth, and D. M. Neumark, *J. Chem. Phys.* **94**, 1740 (1991).
- ¹⁶E. Hirota, K. Kawaguchi, T. Ishiwata, and I. Tanaka, *J. Chem. Phys.* **95**, 771 (1991); T. Ishiwata, I. Tanaka, K. Kawaguchi, and E. Hirota, *ibid.* **82**, 2196 (1985).
- ¹⁷K. Kawaguchi, E. Hirota, T. Ishiwata, and I. Tanaka, *J. Chem. Phys.* **93**, 951 (1990).
- ¹⁸M. Mayer, L. S. Cederbaum, and H. Köppel, *J. Chem. Phys.* **100**, 899 (1994).
- ¹⁹E. Haller, H. Köppel, and L. S. Cederbaum, *J. Chem. Phys.* **78**, 1359 (1983).
- ²⁰See, for example, D. W. Noid, M. L. Koszykowski, and R. A. Marcus, *Annu. Rev. Phys. Chem.* **32**, 267 (1981); E. B. Stechel and E. J. Heller, *ibid.* **35**, 563 (1984); V. E. Bondybey, *ibid.* **35**, 591 (1984).
- ²¹The density of vibrational states in the ground PES near the $^2E'$ origin was obtained by direct harmonic count using the ground state vibrational frequencies from Ref. 8.
- ²²G. Herzberg, *Molecular Spectra and Molecular Structure. III. Electronic Spectra and Electronic Structure of Polyatomic Molecules* (Krieger, Malabar, 1991).
- ²³K. P. Huber and G. Herzberg, *Molecular Spectra and Molecular Structure. IV. Constants of Diatomic Molecules* (Van Nostrand Reinhold, New York, 1979).
- ²⁴W. H. Miller, *Chem. Rev.* **87**, 19 (1987).
- ²⁵Y. S. Choi and C. B. Moore, *J. Chem. Phys.* **97**, 1010 (1992).
- ²⁶H. F. Davis, B. Kim, H. S. Johnson, and Y. T. Lee, *J. Phys. Chem.* **97**, 2172 (1993).
- ²⁷D. W. Kohn, H. Clauber, and P. Chen, *Rev. Sci. Instrum.* **63**, 4003 (1992).
- ²⁸R. E. Smalley, L. Wharton, and D. H. Levy, *J. Chem. Phys.* **63**, 4977 (1975).
- ²⁹E. Böhmer, S. K. Shin, Y. Chen, and C. Wittig, *J. Chem. Phys.* **97**, 2536 (1992).
- ³⁰A. Sanov, C. R. Bieler, and H. Reisler, *J. Phys. Chem.* **99**, 13637 (1995).
- ³¹H. Ni, J. M. Serafin, and J. J. Valentini, *J. Chem. Phys.* **104**, 2259 (1996).
- ³²R. C. Hilborn, *Am. J. Phys.* **50**, 982 (1982).
- ³³H. Okabe, *Photochemistry of Small Molecules* (Wiley-Interscience, New York, 1978).
- ³⁴A number of vibronic level densities have potential relevance for the $^2E' \leftarrow ^2A'_2$ origin region. First, consider all levels of E' vibronic symmetry having one quantum of ν_3 or ν_4 excitation. In this case, $\rho \sim 5/\text{cm}^{-1}$. According to PJT selection rules, these should have the largest coupling matrix elements with the $^2E'$ bright state. Alternatively, counting *all* levels having E' vibronic symmetry yields $\rho \sim 20/\text{cm}^{-1}$, which can be compared to $\rho \sim 100/\text{cm}^{-1}$ for all levels within the $^2A'_2$ electronic state irrespective of vibronic symmetry. The similarity between the density of PJT-promoting-mode levels and the density of mixed levels estimated from the oscillator strength dilution factor is noteworthy. However, this may be fortuitous. For example, since measurements of τ_{fl} values in excess of 100 μs are difficult, it is possible that the zero-pressure lifetimes extend even to the millisecond regime.
- ³⁵I. B. Bersuker and V. Z. Polinger, *Vibronic Interactions in Molecules and Crystals* (Springer-Verlag, New York, 1989).
- ³⁶T. A. Brody, J. Flores, J. B. French, P. A. Mello, A. Pandey, and S. S. M. Wong, *Rev. Mod. Phys.* **53**, 385 (1981).
- ³⁷R. Georges, A. Delon, and R. Jost, *J. Chem. Phys.* **103**, 1732 (1995).
- ³⁸Each of the optically prepared molecular eigenstates contains a large percentage of ground electronic state character as per the oscillator strength dilution factor.
- ³⁹See, for example, V. I. Kukulin, K. M. Krasnopolsky, and J. Horáček, *Theory of Resonances: Principals and Applications* (Kluwer, Dordrecht, 1989); J. A. Beswick and J. Jortner, *Adv. Chem. Phys.* **47**, 363 (1981).
- ⁴⁰P. J. Robinson and K. A. Holbrook, *Unimolecular Reactions* (Wiley, New York, 1972).
- ⁴¹W. Forst, *Theory of Unimolecular Reactions* (Academic, New York, 1973).
- ⁴²W. H. Green, C. B. Moore, and W. F. Polik, *Annu. Rev. Phys. Chem.* **43**, 591 (1992).

- ⁴³W. F. Polik, C. B. Moore, and W. H. Miller, *J. Chem. Phys.* **89**, 3584 (1988); W. F. Polik, D. R. Guyer, C. B. Moore, and W. H. Miller, *ibid.* **92**, 3471 (1990); W. H. Miller, R. Hernandez, and C. B. Moore, *ibid.* **93**, 5657 (1990); R. Hernandez, W. H. Miller, C. B. Moore, and W. F. Polik, *ibid.* **99**, 950 (1993).
- ⁴⁴H. F. Davis, P. I. Ionov, S. I. Ionov, and C. Wittig, *Chem. Phys. Lett.* **215**, 214 (1993).
- ⁴⁵L. D. Landau and E. M. Lifshitz, *Quantum Mechanics* (Pergamon, London, 1958).
- ⁴⁶W. H. Miller, *J. Am. Chem. Soc.* **101**, 6810 (1979).
- ⁴⁷The following ²E' vibrational frequencies were used in calculating densities of states for the 1900–2100 cm⁻¹ interval above the ²E' origin: $\nu_1=773$ cm⁻¹, $\nu_2=944$ cm⁻¹, $\nu_3=1446$ cm⁻¹ (Ref. 8), and $\nu_4=380$ cm⁻¹.
- ⁴⁸I. W. M. Smith, R. P. Tuckett, and C. J. Whitham, *Chem. Phys. Lett.* **200**, 615 (1992).